

Mapping thermokarst lakes and ponds across permafrost landscapes in the Headwater Area of Yellow River on northeastern Qinghai-Tibet Plateau

Raul-David Șerban , Huijun Jin , Mihaela Șerban , Dongliang Luo , Qingfeng Wang , Xiaoying Jin & Qiang Ma

To cite this article: Raul-David Șerban , Huijun Jin , Mihaela Șerban , Dongliang Luo , Qingfeng Wang , Xiaoying Jin & Qiang Ma (2020) Mapping thermokarst lakes and ponds across permafrost landscapes in the Headwater Area of Yellow River on northeastern Qinghai-Tibet Plateau, International Journal of Remote Sensing, 41:18, 7042-7067, DOI: [10.1080/01431161.2020.1752954](https://doi.org/10.1080/01431161.2020.1752954)

To link to this article: <https://doi.org/10.1080/01431161.2020.1752954>



Published online: 30 Jun 2020.



Submit your article to this journal



Article views: 135



View related articles



View Crossmark data



Mapping thermokarst lakes and ponds across permafrost landscapes in the Headwater Area of Yellow River on northeastern Qinghai-Tibet Plateau

Raul-David Şerban ^a, Huijun Jin    ^{a,b,c}, Mihaela Şerban ^a, Dongliang Luo ^a,
Qingfeng Wang^a, Xiaoying Jin    ^{a,d} and Qiang Ma^{a,d}

^aState Key Laboratory of Frozen Soils Engineering, Northwest Institute of Eco-Environment and Resources, Chinese Academy of Sciences, Lanzhou, China; ^bSchool of Engineering and Technology, China University of Geosciences, Beijing, China; ^cSchool of Civil Engineering, Harbin Institute of Technology, Harbin, China;

^dCollege of Resources and Environment, University of Chinese Academy of Sciences, Beijing, China

ABSTRACT

The large variety of the semi-automated methods in mapping the surface water bodies and the frequent omission of ponds (< 10,000 m²) from permafrost regions inventories motivates this work. Based on the correlation matrix, several widely used classification methods for mapping the surface water bodies were assessed. Water bodies inventory was generated at a local and landscape scale in the Headwater Area of the Yellow River (HAYR) on a Sentinel-2 satellite image from 23 November 2015. The assessed methods are: spectral water indices, supervised and unsupervised classifiers (*k*-means, Density Slicing, Maximum Likelihood Classification - MLC), and machine learning algorithms (Random Forest and Support Vector Machines). The MLC method applied on visible and near-infrared (NIR) bands represents the best ratio regarding the accuracy (96%), Kappa coefficient (0.87), and water surface (14.87 km²). However, misclassifications are still present, which requires manual editing. Based on the MLC approach, 651 more water bodies were identified than previous inventories. Ponds are account for up to 93% of the 966 of individual water bodies and contribute to 42% of the total water surface, in the context that were omitted before. This analysis emphasize the importance of method settings for the classifier performance, as well as the ponds abundance and substantial contribution to the total water surface. This inventory will improve the general circulation models and provides baseline information for sustainable management of water resources in the HAYR, one of the core Asian Water Towers.

ARTICLE HISTORY

Received 7 October 2019

Accepted 7 March 2020

KEYWORDS

Remote-sensing mapping;
landscape; thermokarst
lakes/ponds; Headwater Area
of the Yellow River

1. Introduction

Climate change induces rapid and substantial shifts to many Earth systems and earth surface processes, impacting the cryosphere, biosphere, and hydrosphere, especially at high latitudes and elevations (Debeer et al. 2015). This has major societal importance and there are immediate demands for closing this knowledge gaps and for creating predictive

CONTACT Huijun Jin  hjjin@lzb.ac.cn   State Key Laboratory of Frozen Soils Engineering, Northwest Institute of Eco-Environment and Resources, Chinese Academy of Sciences, Lanzhou 730000, China

© 2020 Informa UK Limited, trading as Taylor & Francis Group

tools for environmental management (Debeer et al. 2015). Assessing the dynamics of water bodies at desired spatiotemporal scales and resolutions remains a great challenge for understanding hydrological processes and managing water resources (Du et al. 2016).

One of the most sensitive and critical areas for climate change is the Qinghai-Tibetan Plateau (QTP) in Southwest China. QTP is the highest and largest plateau in the world with an average elevation greater than 4000 m above sea level (a.s.l.) and a surface area of 2.54 million km² (G. Zhang et al. 2017; Wu et al. 2018). In this vast high-elevation region, there are extensive occurrences of glaciers, permafrost, rivers, and lakes, which are important components of the hydrologic cycles (G. Zhang et al. 2017). Lakes cover about 4.01×10^4 km² and glaciers, roughly 4.06×10^4 km² (Guo et al. 2015; Wu et al. 2018).

The underlying permafrost from these areas largely limits the drainage. Thus, the water table is slightly above or below the ground surface. Wetlands are characterized by poor drainage, saturated or moisture-rich soils, and extensive presence of lakes and ponds. Water bodies provide particularly productive habitats in a cold, dry, and usually barren landscape (Muster et al. 2013). These environments play important roles in water, carbon and energy cycling as well in freshwater supply, providing habitats for wildlife (Muster et al. 2017; Rautio et al. 2011). In addition, organic wetland soils, together with water bodies, represent main sources for carbon dioxide (CO₂) and methane (CH₄) emissions to the atmosphere (Euskirchen et al. 2006; McGuire and Anderson 2009). Moreover, in permafrost regions, CO₂ emissions from water bodies, such as thermokarst ponds, are generally higher than the vegetated surfaces (Abnizova et al. 2012).

Water bodies have been mainly mapped using both manual interpretations and digitization of optical data (Yoshikawa and Hinzman 2003; Zhang et al. 2014, 2015; Sun et al. 2018; Luo et al. 2020). Lately, many semi-automatic methods were introduced, such as band thresholding, band rationing, spectral water indices, unsupervised and supervised classifications, or other logic-based methods (Song et al. 2014; Paltan, Dash, and Edwards 2015; Zhang, Chen, and Tian 2018; Li et al. 2019). The Normalized Difference Water Index (NDWI) and the Modified Normalized Difference Water Index (MNDWI) are the most used indices for mapping the surface water bodies (W. Li et al. 2013; Singh et al. 2015; Du et al. 2016; Qiao, Zhu, and Yang 2019). Random Forest (RF) and Support Vector Machines (SVM), all machine learning algorithms, have been extensively used for land cover mapping (Löw et al. 2013; Adam et al. 2014; Clerici, Calderón, and Posada 2017; Räsänen, Elsakov, and Virtanen 2019) and landslides detection (Tien Bui et al. 2016; Ghorbanzadeh et al. 2019). Recently, these algorithms were adopted in remote sensing applications for permafrost modelling (Deluigi, Lambiel, and Kanevski 2017; Wang et al. 2019a) and surface water body mapping (Lv, Yu, and Yu 2010; Rokni et al. 2015; Wang and Xu 2018; Zhang, Chen, and Tian 2018). Unsupervised (k-means) and supervised classifiers (Density Slicing – DS and Maximum Likelihood Classifier – MLC) were extensively used in terrain classification and water body mapping in the Arctic regions (Grosse, Schirrmeyer, and Malthus 2006; Muster et al. 2012, 2017; Lara et al. 2015; Paltan, Dash, and Edwards 2015). All these semi-automatic methods have reported accuracies varying on a wide range from 48% to 99%. These accuracies depend on the spectral and spatial properties of remote-sensing imagery, method settings, sensor characteristics, and time of acquisitions (Muster et al. 2017; Zhang, Chen, and Tian 2018). Extensive applications of a specific method at different sites remain challenging because of the parameter tuning issues for diverse contexts (Yang et al. 2015; Zhang, Chen, and Tian 2018). Specifically, lake boundary pixels representing a mixture of land and water

pose problems for classification, as the spectral signature of the pixel is hard to distinguish (Muster et al. 2013; Andresen and Lougheed 2015).

Most studies have used Landsat and Moderate Resolution Imaging Spectroradiometer (MODIS) imagery. Their main shortcoming is the exclusion of small lakes, leading to an underestimation of water surface extent (Carroll et al. 2011; Boike et al. 2016; Kravtsova and Rodionova 2016; Zhang, Li, and Zheng 2017; Sun et al. 2018). Moreover, ponds with water surface area smaller than 10,000 m² have been frequently omitted from water body inventories (Muster et al. 2017). Mainly lakes larger than 1 km² were mapped on regional studies on the QTP (Zhang et al. 2014, 2017; Wan et al. 2016; Lu et al. 2017; Sun et al. 2018). Zhang et al. (2014) developed the first inventory of lakes on the QTP in which water bodies as small as 1000 m² were mapped. These features were manually digitized on the GeoCover Landsat mosaic 2000 with a pixel size of 14.25 m (Zhang et al. 2014). Unfortunately, statistics on the pond category was not conducted and only lakes larger than 1 km² were analysed. However, the importance of small lakes for climate change through biogeochemical processes is widely recognized. A local study covering 2,513.6 km² on the interior QTP has mapped water bodies as small as 1000 m² on SPOT images from 2010 at a 10 m spatial resolution (Luo et al. 2015). In their case, ponds (from 1000 to 8000 m²) represented 47% of the total water bodies (Luo et al. 2015). Recently, ponds have attracted wide attention, because they contribute substantially to biological activities and CO₂ and CH₄ emissions (Smol and Douglas 2007; Laurion et al. 2010; Abnizova et al. 2012; Kuhn et al. 2018). A study from Siberian tundra has proved that ponds omission from wetlands mapping leads to an underestimation of CO₂ emissions by 35% on average and up to 62% (Abnizova et al. 2012). However, their effects on carbon emissions remain difficult to quantify as a result of lacking accurate maps of ponds in many permafrost regions (Muster et al. 2013). Thereby, accurate mapping will improve water resource management and the general circulation models that currently treat surface water in an overly simplified manner (Pekel et al. 2016).

Ponds inventories have started to be compiled from a local to a regional scales in the Arctic regions with a resolution of ≤ 6 m (Andresen and Lougheed 2015; Liljedahl et al. 2016; Muster et al. 2017; Cooley et al. 2019). Ponds dominate the Arctic lowlands, comprising up to 95% of individual water body number, and accounting for up to 30% of total water surface area (Muster et al. 2012, 2013). A recent global high-resolution mapping approach has been conducted by using Landsat satellite imageries, but water bodies smaller than 900 m² haves not yet been included (Pekel et al. 2016). Taking into account that the minimum size for a reliable feature identification it is 4 or 5 pixels (Schneider, Grosse, and Wagner 2009; Williamson et al. 2018; Muster et al. 2017), the threshold area of the smallest mapped ponds are theoretically set at 3600 m². Our challenge is to improve this lower boundary by using the recently free-available Sentinel-2 imageries at 10 m spatial resolution for mapping surface water bodies.

The purpose of this study is to compile an inventory of lakes and ponds from Sentinel-2 remote-sensing data. Taking the Headwater Area of the Yellow River (HAYR) as an example, this inventory at a landscape scale will complement previous approaches and will improve the existing databases of surface water bodies on the QTP. The main objectives are to: (i) Produce 10 m water-body datasets from Sentinel imagery; (ii) Compare and evaluate the accuracy of different classification techniques, and; (iii) Evaluate the number and size of surface water bodies.

2. Materials and methods

2.1. Study area

The study area covers an area extent of 150 km² at Chalaping (34°13'N, 97°48'E; from 4544 to 4853 m a.s.l., with a mean of 4640 m a.s.l.) in the south-central part of the HAYR on NE QTP. The HAYR is part of the Sanjiangyuan (Source Area of the Three Rivers – SATRs: Yangtze, Yellow and Lancang-Mekong rivers) National Park of China. Chalaping is situated at the north of the Bayan Har Mountain Pass along the National Highway G214 in the upper stream of Reqü River ([Figure 1](#)). Geomorphologically, this area represents a high plateau cut by the Reqü River in the southeastern part and by a small creek in the western side.

Glacial deposits, together with the periglacial features, such as thermokarst lakes, pingos, and palsas, are present extensively in this area ([Jin et al. 2009](#)). Numerous thermokarst lakes and ponds occur in valleys and depressions. Permafrost is well developed at Chalaping with ground temperatures measured at the depth of zero annual amplitude (generally from 10 to 25 m in depth) between – 2 and – 1°C. Permafrost thickness ranges from 60 to 100 m, and the active layer thickness is generally less than 1 m in areas of organic soil surface ([Luo et al. 2018a, 2018b](#)). Vegetation is predominantly alpine meadow and alpine paludal meadow, and the substrate is characterized by fine-grained soil with a mix of organic and humus layer, sand and coarse gravel ([Luo et al. 2018b](#)). The climate is cold and semi-arid at the northern flank of the Bayan Har Mountains. At the Chalaping measurement site, mean annual air temperatures range from – 5.1 to – 3.8°C, with annual precipitation of 460 mm from 2011 to 2016 ([Luo et al. 2018a](#)).

2.2. Data acquisition and image preprocessing

Methodology workflow consists of data acquisition, preprocessing of the satellite images, and generation of water bodies extent using different classification techniques ([Figure 2](#)). The results were quantitatively assessed and compared. Finally, the number and size of water bodies were evaluated.

The satellite image used in this study is the recent European Space Agency Sentinel-2A product. Sentinel-2 Multi-spectral Instrument (MSI) provides radiometrically and geometrically multi-spectral images by compiling 13 bands with spatial resolutions from 10 to 60 m. These bands cover the visible, near-infrared (NIR), and short-wave infrared (SWIR) of the electromagnetic spectrum ([Clerici, Calderón, and Posada 2017](#)).

Water body surface area may be affected by the total amount of precipitation prior to image acquisition ([Jones et al. 2011](#)). Summer precipitation represents 57.7% of the annual total precipitation at Chalaping ([Luo et al. 2018a](#)). In addition, summer is the peak growth period for aquatic plants; this impacts the classification or the delineation of shorelines, especially for shallow water bodies ([Jones et al. 2011; Muster et al. 2017](#)). Other seasonal processes, such as snowmelt, evaporation, advancing of ground thaw depth, and the onset of lake-ice break-up and freeze-up, may also influence the surface measurements ([Jones et al. 2011; Muster et al. 2017](#)). The water surface of lakes on the QTP becomes relatively stable in autumn and is less ice covered ([Song et al. 2014](#)). Moreover, satellite imageries have a lower degree of cloud coverage in autumn ([Song et al. 2014](#)). Therefore, the satellite imageries were acquired between

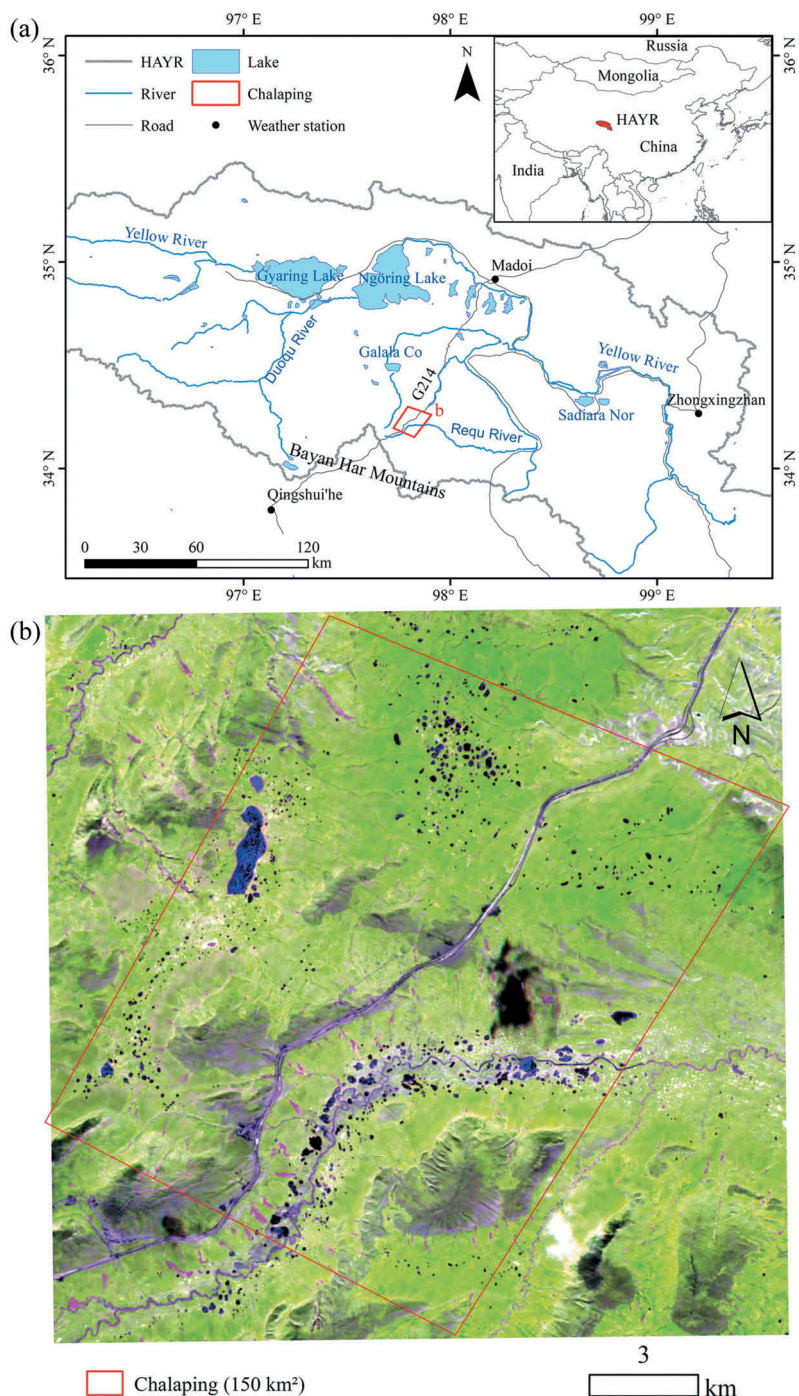


Figure 1. Study area location at Chalaping: (a) in the south-central part of the HAYR; (b) Sentinel-2 MSI image from 23 November 2015 of the investigation area (band combination 8-11-4).

late summer and mid-autumn (September–November), excluding the snowmelt and rainy summer season. In addition to these criteria, the images used in this study were

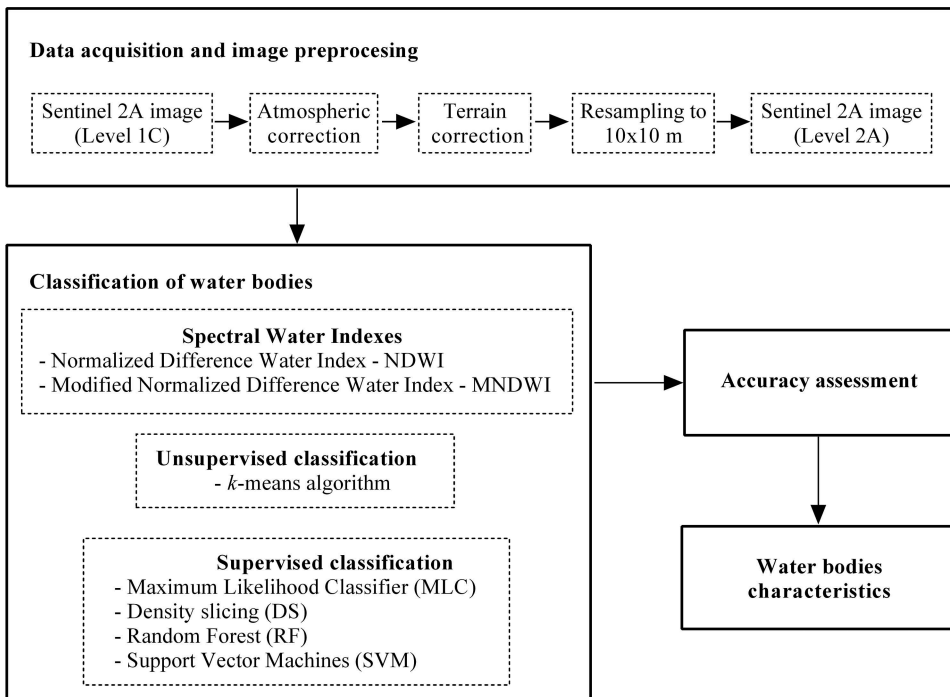


Figure 2. Summary of the steps applied to Sentinel-2 input data in order to extract the water bodies distribution by assessing different remote sensing classification methods.

selected also on the basis of: (a) Similar acquisition dates in accordance with the GeoEye reference image from Google Earth acquired on 22 September 2015; (b) Quality of the image, e.g. clear sky or less cloudy, and; (c) Common footprint.

Because the Sentinel mission started in the second half of 2015, only two scenes from autumn 2015 were available for this area. The scene from 23 November was used because of less snow coverage on slopes and less lake-ice coverage. Additionally, it had one cloudy case in the study area that gave the opportunity to test the classifiers in all weather conditions, including the cloudy sky. The dataset was downloaded from the European Space Agency (ESA) Pre-Operations Hub (<https://scihub.copernicus.eu/>). A digital elevation model (DEM) with a spatial resolution of 12.5 m, generated from the Phase Array type L-band Synthetic Aperture Radar (PALSAR) microwave sensor on-board the Advanced Land Observing Satellite (ALOS), was downloaded from Alaska Satellite Facility (<https://www.asf.alaska.edu/>). This DEM was used for image terrain corrections and as an additional layer in some classifications.

Preprocessing of satellite images and the water bodies classification were performed by using the Sentinel Application Platform (SNAP, version 6.0.4). Only the SVM algorithm was performed in ENVI 5.3 software. Sentinel-2A Level-1 C dataset is a Top-Of-Atmosphere (TOA) standard product. On this product, atmospheric and terrain corrections were applied using the ESA Sen2Cor toolbox (version 2.5.5). As a result, the Level-2A Bottom-Of-Atmosphere (BOA) product was obtained (Main-Knorn et al. 2015). All bands were resampled at 10 m spatial resolution and a subset of 150 km² was extracted for the study area (Figure 1).

2.3. Classification of water bodies

Several well-known and widely-used remote sensing mapping methods, including supervised and unsupervised classifications and spectral water indices, were applied and assessed.

2.3.1. Spectral water indices

The NDWI is one of the most used indices in the last decades due to its simplicity and efficiency (McFeeters 1996; W. Li et al. 2013; Singh et al. 2015; Qiao, Zhu, and Yang 2019). NDWI is based on the principle that water bodies have strong absorability in the green visible band (G) and low radiation in the NIR band (McFeeters 1996). It is calculated as:

$$\text{NDWI} = \frac{G - (\text{NIR})}{G + (\text{NIR})} \quad (1)$$

where G is the TOA of Band 3 and NIR is the TOA of Band 8 for Sentinel-2A.

The principal shortcoming of NDWI is that it is sensitive to built-up structures and often over-estimates the water bodies. To reduce this limitation, Xu (2006) developed the MNDWI by replacing the NIR band with the SWIR band. This replacement is made because in the SWIR band water bodies have a stronger absorability than in the NIR band, and the build-up land has considerable radiation in the SWIR band than in the NIR band (Xu 2006; Du et al. 2016). Thus, the MNDWI is defined as:

$$\text{MNDWI} = \frac{G - (\text{SWIR})}{G + (\text{SWIR})} \quad (2)$$

where G is the TOA of Band 3 and SWIR is the TOA of Band 11 for Sentinel-2A.

2.3.2. Unsupervised classification

Unsupervised classification is the process of automatic grouping of pixels with similar spectral characteristics (Lillesand, Kiefer, and Chipman 2004). The k -means unsupervised classifier is an iterative clustering algorithm that maximizes the between-cluster variance and minimizes the within-cluster variability based on the following equation (Muster et al. 2012):

$$SS = \sum_{\forall x} [x - C(x)]^2 \quad (3)$$

where the between-cluster variance is defined as the sum of squared distances SS between each pixel x and its assigned cluster centre $C(x)$ (Muster et al. 2012).

A k -means clustering algorithm was applied for different band combinations: all bands; blue (B), red (R), G and NIR; or just NIR or SWIR. Moreover, various settings were tested regarding the number of classes (from 3 to 14) and iterations (10, 15, and 30).

2.3.3. Supervised classification

The MLC is one of the most widely used supervised methods for land cover classification. This algorithm unites pixels with similar reflectance across the multispectral space based on statistical models derived from the input training samples (Lara et al. 2015). The model assumes that the conditional probability distribution function is normally distributed (Lillesand, Kiefer, and Chipman 2004). The MLC was applied using two to four classes and

on all bands, or just for *B*, *G*, *R*, and NIR bands. The DEM and the Normalized Difference Vegetation Index (NDVI) were also added in the classification. NDVI is an indicator for chlorophyll density and is calculated from the *R* and NIR band (Johansen and Tømmervik 2014):

$$\text{NDVI} = \frac{R - (\text{NIR})}{R + (\text{NIR})} \quad (4)$$

where *R* is the TOA of Band 4 and NIR is the TOA of Band 8 for Sentinel-2A.

DS is another supervised method for separating water from other classes by setting a threshold on the NIR band. This method is useful for high-resolution images to detect features much larger than pixel size (Knight, Tindall, and Wilson 2009). The utility of this technique is that the feature class is categorically defined and can be used repeatedly when the spectral properties of the feature are rather constant (Knight, Tindall, and Wilson 2009). The NIR band is particularly useful for identifying water bodies, as most of the incoming solar radiation is absorbed. Thus, this provides a clear difference between the reflectance from water surfaces and from the other features (Muster et al. 2012; Lu et al. 2017).

Multiple approaches were applied for setting the proper threshold for the NIR band. First, it was based on the statistics from the water bodies training set, including quartiles, histogram, and 3 Sigma rule. Moreover, 82 pixels were digitized from one lake at different depths based on pixels reflectance intensity. Darker pixels from the centre of the lake represent larger water depths while brighter pixels close to the lake shore represent shallow depths. Different thresholds were tested on the basis of the minimum, maximum, and average values of these samples. Finally, in combination with the visual checking, a threshold was established for recording the highest accuracy after the validation stage.

RF is a supervised classification algorithm developed for machine learning (Breiman 2001). It has been recently adopted for remote sensing applications (Gislason, Benediktsson, and Sveinsson 2006; Veronesi and Hurni 2014; Deluigi, Lambiel, and Kanevski 2017; Wang et al. 2019b). In comparison with the traditional supervised classifiers, RF is an ensemble learning algorithm for computing multiple binary classification trees that are combined to generate a classification. The RF uses the principle of Classification And Regression Trees (CART) developed from a random resampling of the input data with the replacement of the predictive variable sets (Breiman 2001; Peters et al. 2007).

Aggregating a high number of trees usually increases the accuracy and makes the model more robust to noise (Gislason, Benediktsson, and Sveinsson 2006; Deluigi, Lambiel, and Kanevski 2017). Thus, two main parameters need to be set: the number of trees and that of predictive variables for splitting the nodes. Similar to MLC method, the RF was applied using two to four classes and different band selection, together with DEM and NDVI. We used 2/3 bootstrap of the training data to build the trees, and the remaining was used to assess the generalization error of the algorithm (Deluigi, Lambiel, and Kanevski 2017). We started with 10 trees and stopped at 500 trees because the generalization error (out-of-bag error) became stable after 300 trees.

SVM is a non-parametric learning algorithm, member of the kernel methods, which derived from statistical learning theory (Burges 1998; Vapnik 1999). This algorithm principle is that the training vectors are linearly separated by an optimal hyper-plane into a higher-dimensional space through the non-linear transformers. The optimal hyper-plane will be

established when the separating margins between the training vectors are maximal (Janik and Lobos 2006; Deluigi, Lambiel, and Kanevski 2017). These maximum separating margins are called support vectors (Ghorbanzadeh et al. 2019). The classification results depend of the kernel function as the kernel controls the complexity of the mapping (Deluigi, Lambiel, and Kanevski 2017).

Using the same training set as for the MLC and RF methods several kernel types were tested (e.g. linear, Polynomial, Sigmoid, and Radial Basis Function – RBF). Different values ranging from 10^{-5} to 10^1 as well as 10^{-1} to 10^5 were tested for optimizing *gamma* (*γ*) and *C* parameters. Pyramid parameter and probability threshold were set to zero, meaning that the image will be processed at full resolution and no unclassified pixels will result. SVM was tested on two classes and on different band selection.

2.4. Validation and accuracy assessment

The validation and training sets consist of 163 polygons larger than 400 m^2 manually digitized on two high-resolution GeoEyes images available from the Google Earth. The GeoEyes images were acquired on 22 September 2015 with two spatial resolutions of 0.42 and 0.47 m (<https://discover.digitalglobe.com/>, 5 September 2018). All the polygons were overlaid on the Sentinel-2 scene from 23 November 2015 and their matches were visually checked. These polygons are representative and uniformly distributed inside the study area. They were randomly split in two subsets with an 80:20 ratio, which is frequently used in statistically based classifications (Van Den Eeckhaut et al. 2006; Bai et al. 2010; Nitze, Schultheiss, and Asche 2012). The 80% represents the training set with 62 water body polygons (1858 pixels) and 69 without (6676 pixels), while the 20% represent the validation dataset. Usually, acquiring a large and high-quality training set is costly and time-consuming, especially for large study areas. In this context, recent works demonstrated the potential for accurate classification of the machine learning algorithms by using small training sets (Pal and Foody 2012; Tien Bui et al. 2016; Clerici, Calderón, and Posada 2017). The training dataset was used for generating the MLC, to train the RF and SVM algorithms, and for establishing the thresholds for DS.

Although the derived validation dataset represents just 32 polygons, it covers 1495 pixels at a 10 m spatial resolution. These validation pixels represent a variety of land types (grasslands, bare ground, and anthropic constructions) and lakes of different sizes across the study area. Moreover, the 1495 validation pixels cover the entire surface of the lakes and are not sporadic pixels inside the lakes. Thus, the lakes margins, usually problematic for lakes mapping, are also taken into account. Several water body mapping studies from the Arctic regions show that 30 to 40 representative validation points are adequate even for larger study areas (Andresen and Lougheed 2015; Lara et al. 2015).

Classification accuracy was assessed for every classification result based on the confusion matrix and its derived indices: commission and omission errors, overall accuracy, and Kappa coefficient. Overall accuracy (OA), producer's accuracy (PA) and user's accuracy (UA) were generated by using the following equations:

$$\text{OA} = \frac{(\text{TP}) + (\text{TN})}{P + N} \quad (5)$$

$$PA = \frac{(TP)}{(TP) + (FN)} \quad (6)$$

$$UA = \frac{(TP)}{(TP) + (FP)} \quad (7)$$

where P and N are real positives (water surface) and negatives (others), TP and TN are true positives and negatives, and FP and FN are false positives and negatives (Frantz et al. 2018). OA is the sum of correctly classified pixels for every class, and it is divided by the total number of pixels. PA is the probability that true pixels are correctly classified and thus includes only errors of omission (water bodies underestimated). UA is the probability that mapped pixel labels are correct and includes only errors of commission (water bodies overestimated) (Verpoorter, Kutser, and Tranvik 2012; Pekel et al. 2016). Thereby there are four possible cases: pixel with known water presence is predicted correctly (TP); water absence is predicted correctly (TN); water presence is not detected (FN), and; water absence is incorrectly predicted (FP) (Deluigi, Lambiel, and Kanevski 2017).

Another discrete multivariate technique in accuracy assessment is the Kappa coefficient (K), computed as:

$$K = \frac{N \sum_{i=1}^r rx_{ii} - \sum_{i=1}^r r(x_{i+} \times x_{+i})}{N^2 - \sum_{i=1}^r r(x_{i+} \times x_{+i})} \quad (8)$$

where N is the total number of observations; r is the number of rows in the matrix; x_{ii} is the number of observations in the row i and column i ; x_{i+} is the total for row i , and; x_{+i} is the total for column i (Congalton 1991). K indicates whether the values contained in the confusion matrix represent a result significantly better than random (Verpoorter, Kutser, and Tranvik 2012). Situations of $K > 0.8$ indicate perfect agreement; 0.6–0.8, substantial; 0.4–0.6, moderate; 0.2–0.4, fair, and; < 0.2 slight (Landis and Koch 1977).

The classified images were converted from raster format to vector shapes in order to derive the water body statistics. Validation steps and extracting the morphometric characteristics (number, size, and surface extent) of water bodies were performed in ArcGIS v10. Water bodies smaller than 400 m^2 that cover four pixels of Sentinel imagery were excluded from the analysis.

3. Results

3.1. Accuracy assessment of water body classification

Overall, 104 classifications were performed, with 37 comparable results (Figure 3(a)): two results from the NDWI and MNDWI, eight from the unsupervised classifier, eight from DS, seven from MLC, seven from SVM, and five from RF. Detailed information of every classification settings and codes is presented in Table S1. Almost all the classifiers presented an OA $> 80\%$, while MLC5, RF9, and RF16 reached 96%. The exceptions were k -means8 and k -means11 with an OA of 79% and 78%, respectively. Regarding the K , more than one-half of the results presented a substantial agreement (Figure 3(a)). These classifications were mainly generated by the k -means ($n = 6$), DS ($n = 6$), and SVM techniques ($n = 5$). A perfect agreement was recorded just by MLC ($n = 6$), RF ($n = 3$),

and SVM1 methods. NDWI and SVM34 showed a moderate agreement, while MNDWI and *k*-means11, a fair agreement. Only *k*-means8 presented a slight agreement ($K < 0.2$).

The coefficient of determination indicate a high correlation ($R^2 = 0.88$) between OA and K , while these indices do not correlate with the water body surface (Figure 4). Almost one-half of the classifiers recorded a total water surface area up to 10 km^2 (Figure 3(b)). They included the water indices, all the *k*-means results, one-half of the DS, and SVM34. The NDWI revealed the lowest total water surface area of 4.06 km^2 , followed by the *k*-means classifiers, which started from 4.13 km^2 . MLC ($n = 6$), SVM ($n = 6$), RF9, RF11, and the other half of the DS results presented a total water surface area ranging from 10 to 30 km^2 . The water bodies total surface area generated by the RF method ($n = 3$) and DS7 exceeded 30 km^2 , while the MLC4 provided the maximum extent of water (45.9 km^2).

Maps of water body distribution resulted from these classifications show large misclassifications of water extent generated by supervised classifiers, especially the RF (Figure 5(a)). RF9 results presented the highest OA and K , and implicitly a high PA and UA (>90%), and low commission and omission errors (<10%) (Table S1). In the same time, it generated a high surface of water bodies (25.54 km^2). On the contrary, the NDWI produced the smallest area for water bodies (4.06 km^2) and still had a high OA and a moderate agreement for K (Figure 5(b)). Even so, the omission error was high as 55.9%, suggesting a large underestimation of the water bodies (Table S1). MLC5 reached also the highest OA (96%) and a perfect agreement, with a total water surface area of 14.87 km^2 (Figure 5(c)). The DS13 method showed a slight decrease in OA and a substantial decrease in K , while the water surface was reduced by up to 5.43 km^2 (Figure 5(d)). Meanwhile, DS13 result still presented a high OA (90%) and a substantial agreement ($K > 0.71$). SVM1 reveal one of the highest OA (94%) and a perfect agreement, but generated also larger areas of surface water bodies (Figure 5(e)). The unsupervised classification *k*-means18 presented results comparable to the NDVI with slightly higher accuracy and surface for the water bodies (Figure 5(f)).

The misclassifications, especially affecting the unsupervised and supervised classifications, were caused by the presence of shadows, snow, and ice. Shadows were not completely removed after the atmospheric and topographic corrections. Low altitude clouds are often undetectable by the Sentinel-2 cirrus band (Frantz et al. 2018). The road is also mixed-up with water bodies for the RF, MLC, and to some extent for *k*-means as well.

3.2. Number and dimensions of lakes and ponds

From here, we will present the water bodies characteristics generated by the NDWI and MLC5. The NDWI indicated the lowest misclassification, a high OA and a moderate agreement, but a high omission error as well. The MLC5 presented similar results with RF9 for assessing their accuracy but with a water surface area smaller with 10.7 km^2 .

In many cases, NDWI results underestimated the water body boundaries and generated spurious pixels within the water bodies surface area. Thereby, a mean filter of 3×3 cells was required to remove the spurious pixels and to extend the water boundaries according to their reference polygons. This was unnecessary for the MLC5 method. After applying the filter, the OA increased from 87% to 90% and the K from 0.55 to 0.69, providing a substantial improvement. In addition, water body surface increased to 6.4 km^2 . A refining procedure was necessary for removing the misclassifications (shadows, snow, ice, roads, and rivers), especially for MLC5. In addition, water bodies smaller than

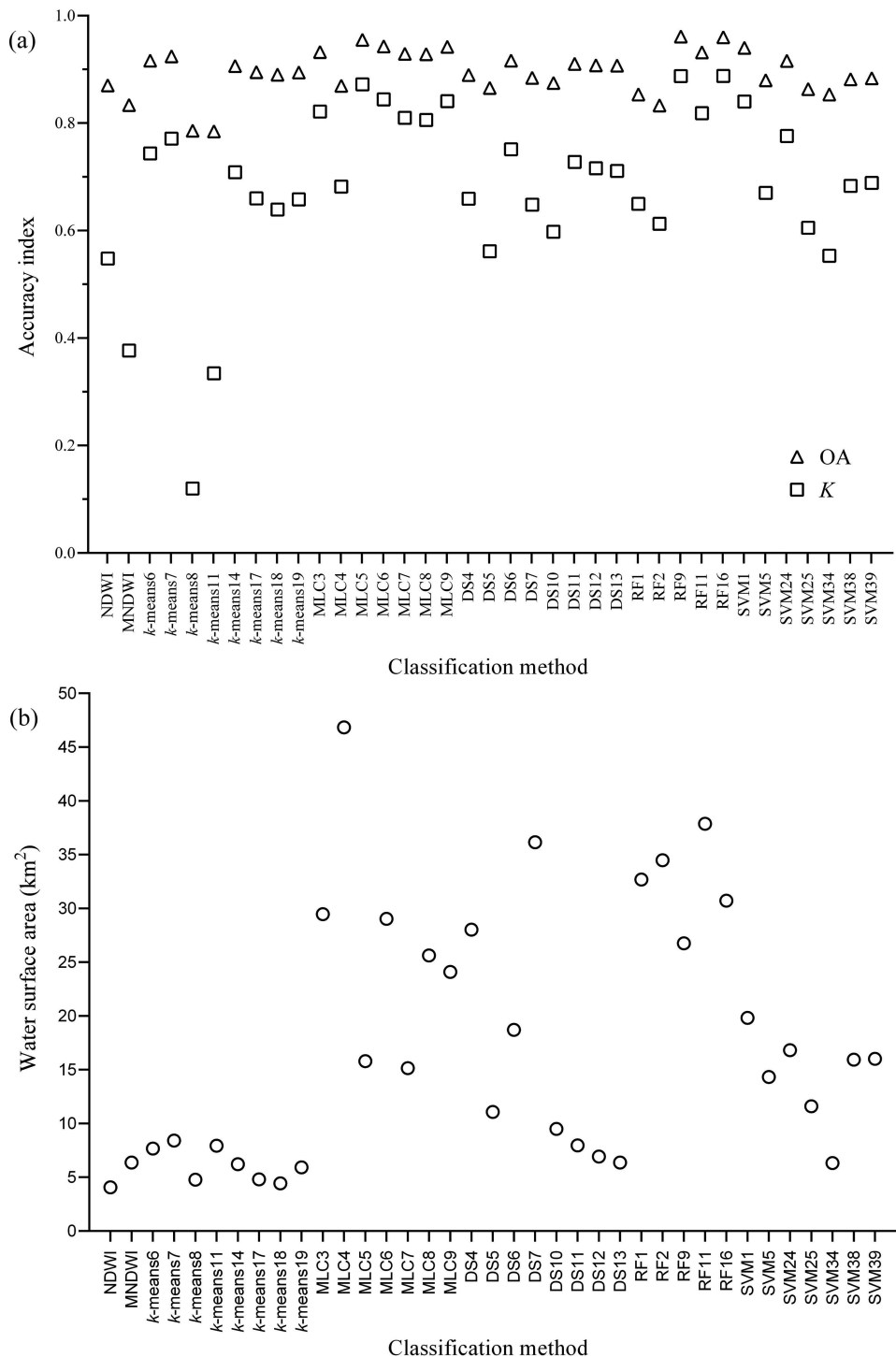


Figure 3. Confusion matrix indices for the 37 compared classifications: (a) OA is represented in percentage and K in values range from 0 to 1; (b) Water bodies surface area is represented in km².

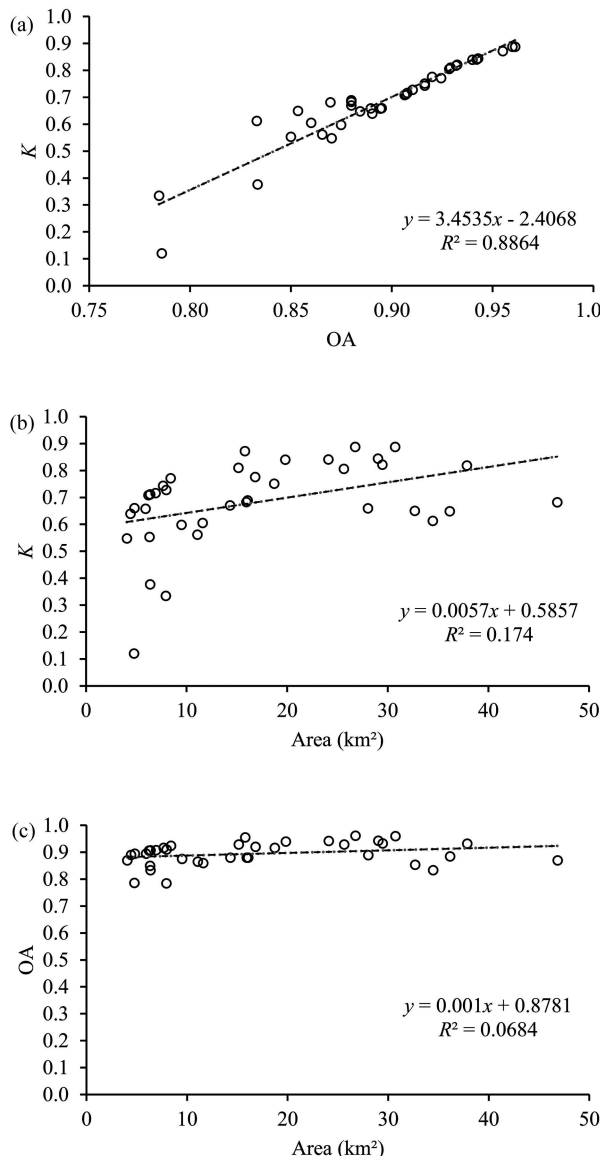


Figure 4. Comparison of the regressions between accuracy indices: (a) K and OA; (b) K and water bodies surface; (c) OA and water bodies surface.

400 m^2 and those mapped outside the study area were removed. Finally, the NDWI identified 528 water bodies, covering a total water surface area of 3.82 km^2 , while the MLC5 method detected 966 water bodies with a total water surface of 4.7 km^2 .

Related to their area, water bodies were divided into three classes: ponds ($< 1 \text{ ha}$), small lakes (1 to 10 ha), and large lakes ($> 10 \text{ ha}$). Both methods mapped the three large lakes, while MLC5 identified four small lakes more than NDWI (Figure 6(a)). The difference was made by the ponds where the supervised classifier detected 434 more ponds than the NDWI. There were 517 common water bodies mapped by both methods. The NDWI

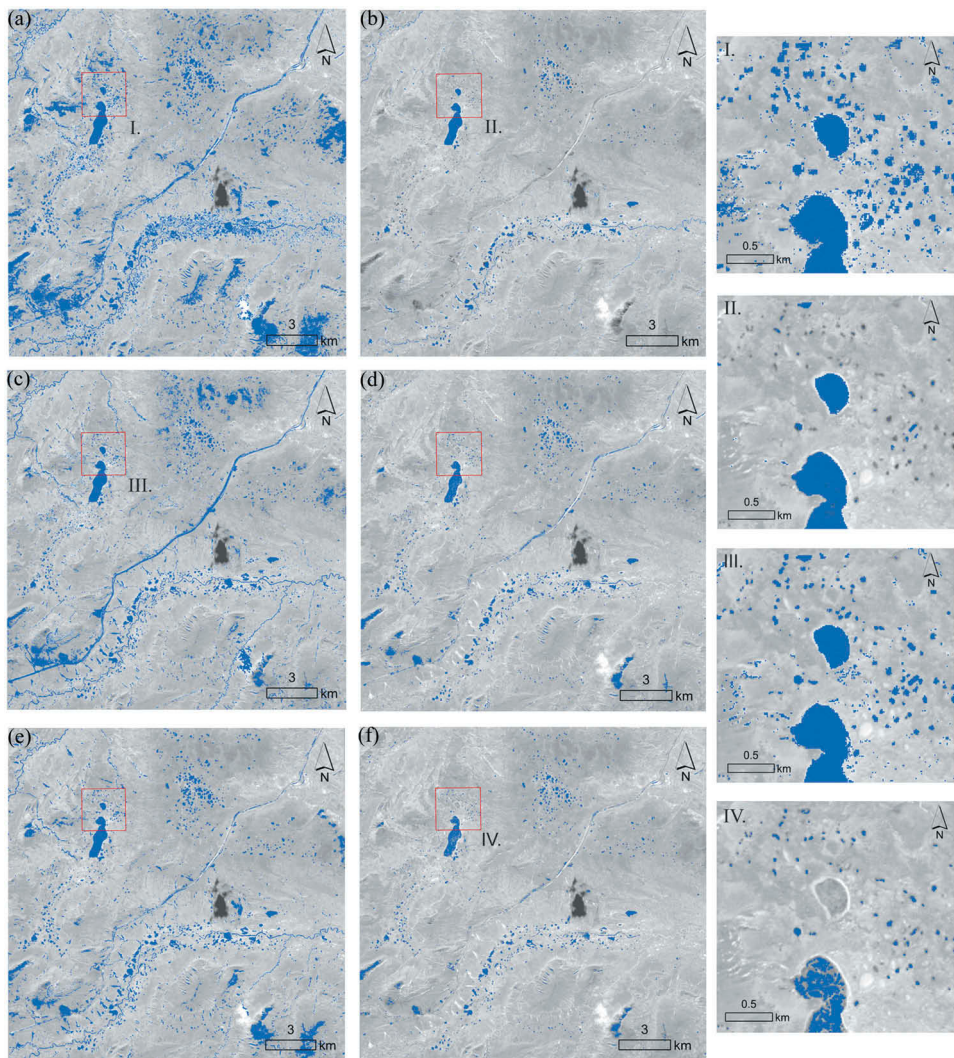


Figure 5. Water body distribution maps overlaid on the NIR band resulted from the compared classifications: (a) RF9: OA = 96%, K = 0.89, $S = 25.54 \text{ km}^2$; (b) NDWI: OA = 87%, K = 0.55, $S = 4.06 \text{ km}^2$; (c) MLC5: OA = 96%, K = 0.87, $S = 14.87 \text{ km}^2$; (d) DS13: OA = 91%, K = 0.71, $S = 5.43 \text{ km}^2$; (e) SVM1: OA = 94%, K = 0.84, $S = 19.82 \text{ km}^2$; (f) k-means18: OA = 89%, K = 0.64, $S = 4.13 \text{ km}^2$. Classification settings are detailed in Table S1. S = surface area of water bodies, and I. to IV. = insets of a zoomed view.

detected only 11 features more than MLC5, while MLC5 mapped 449 more water bodies than NDWI, especially in the pond category. Together, these two methods mapped 977 water bodies. Thereby, since the omission error was larger than 50%, the NDWI method showed a substantial underestimation of the water bodies (Figure 7(c)). On the contrary, MLC5 showed an overestimation of water bodies, but after the visual refinement, the mapped water bodies were closely matched with reality (Figure 7(d)). Thus, based on MLC5, the three largest lakes cover 1.19 km^2 , while the 61 small lakes cover 1.56 km^2 (Figure 6(b)). The largest lake from the study area with a surface of 0.93 km^2 represents

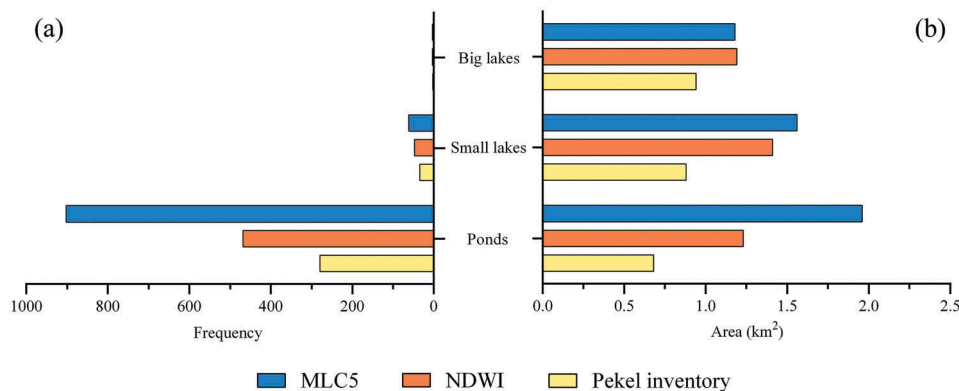


Figure 6. Comparison of the water bodies generated by MLC5 and NDWI with the inventory of Pekel et al. (2016): (a) Frequency; (b) Surface area. Water bodies are divided into three classes based on their size: ponds (< 1 ha), small lakes (1 to 10 ha), and large lakes (>10 ha).

19.7% of the entire water surface. With 902 features, the ponds category covers a total water surface of 1.96 km². Ponds constitute up to 93% of individual water bodies and contribute to 42% to the total water surface.

4. Discussion

4.1. Classification accuracy

By comparing these classification methods on the same spatial and spectral conditions, differences were observed regarding their accuracy, especially in water extent. Differences occurred even for the same method, depending on method tuning. For example, MLC5, which revealed the best ratio regarding the accuracy (96%) and water surface (14.87 km²), mapped two classes using four bands (visible and NIR bands) (Table S1). Adding NDVI, DEM or other bands in the classification decreased the OA and K but increased water surface. Moreover, changing to four classes substantially increased the water bodies surface area as revealed by MLC4. On the contrary, by using four classes, 15 iterations, and all the bands, the *k*-means7 produced the highest OA and K for unsupervised classification. This setting also revealed the largest water extent (7.29 km²) for this method. Using just the NIR band and increasing up to seven classes, the water surface decreased to 4.13 km². OA slightly decreased to 89% and K to 0.64. Muster et al. (2012) obtained good results by applying the *k*-means algorithm on the NIR band using 9 classes and 15 iterations. Luo et al. (2015) applied this unsupervised classifier on the SWIR band for thermokarst lakes mapping on the QTP but did not mention their obtained accuracy. In our study, using the SWIR band decreased both the OA and K to 89% and 0.66, respectively (*k*-means19 in Table S1). Palmtag et al. (2016) applied the MLC method with the same band selection as in our case, but on QuickBird-2 images (2.4 m). However, they obtained an accuracy ranging from 77% to 90%.

Two classes, 300 trees, NDVI and almost all bands (without B1, B9, and B10) were the best settings for the RF method (RF9 in Table S1). Adding the DEM into the classification, or increasing the tree number, just expanded lake surface area. For the DS method, the

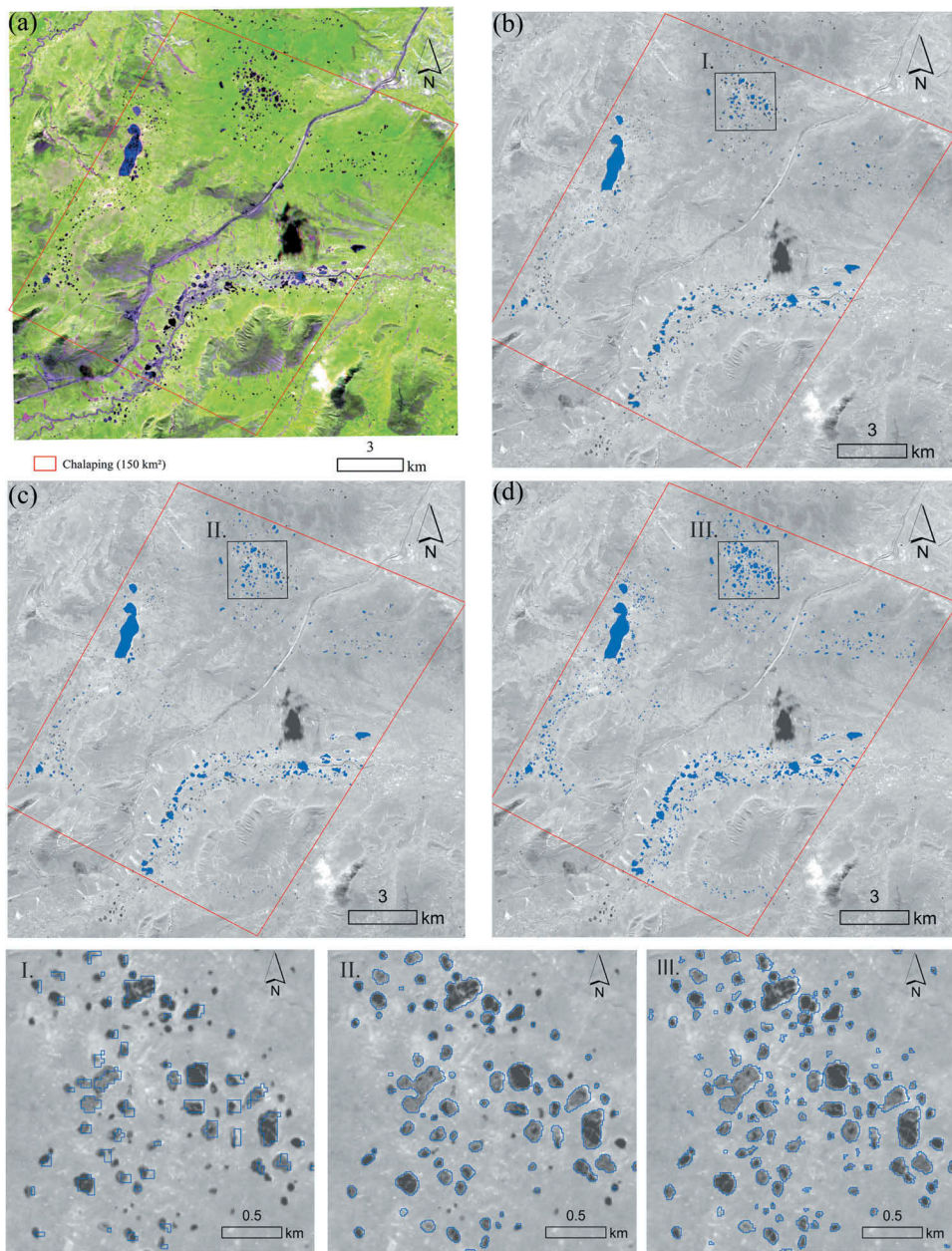


Figure 7. Water body distribution maps overlaid on the NIR band after the refining step: (a) Sentinel-2 MSI image (band combination 8-11-4); (b) Inventory of Pekel et al. (2016); (c) NDWI; (d) MLC5; I. to III. = insets of a zoomed view.

best results ($OA = 91\%$) were obtained by using a threshold on NIR band based on the values sampled from one lake (WBI38) and visually adjusted. Other approaches to set the threshold revealed slight decreases in accuracy indices and increases in lake water surface

area. Paltan, Dash, and Edwards (2015) applied the same method on Landsat SWIR band and obtained an accuracy of 80%.

SVM algorithm applied on all bands using RBF kernel with a γ and C parameters of 0.083 and 100, respectively, reached the highest accuracy (SVM1 in Table S1). In the same time, mapped the largest surface area of the water bodies for this method. Changing the bands number, the γ and C parameters, as well as the kernel type lead to a significant decrease of the K and the water bodies total surface area. As in many other studies (Rokni et al. 2015; Deluigi, Lambiel, and Kanevski 2017; Zhang, Chen, and Tian 2018; Räsänen, Elsakov, and Virtanen 2019), RBF was proven the most robust kernel function. Several studies reported accuracies up to 99% for the SVM method, but used in combination with other techniques and for mapping large water areas (Lv, Yu, and Yu 2010; Rokni et al. 2015; Wang and Xu 2018). For example, Wang and Xu (2018) mapped a large lake by using all Landsat-8 bands and obtained a K of 97%. However, in terms of mapping glacial lakes with various sizes, the SVM classifier generated considerable overestimations of the lakes area (Zhang, Chen, and Tian 2018).

Numerous previous studies have shown that MNDWI better extracts water features than NDWI, efficiently suppress and even remove the build-up structures, vegetation and soil noise (Xu 2006; Li et al. 2013; Singh et al. 2015; Du et al. 2016). In our case, the NDWI ($OA = 87\%$, $K = 0.55$) performed better than MNDWI ($OA = 83\%$, $K = 0.38$), (Table S1). This may be explained by the lack of built-up area at our study site, which has not affected the classification. Thus, replacing the NIR band with the SWIR band did not improve the water index results, at our study site. Similarly, inclusion of the SWIR band did not improve results in the unsupervised classifications. Omission error suggests that small ponds are not detected due to the low spatial resolution (Table S1). Even for images of 4 m resolution, the omission errors can occur (Muster et al. 2013). Commission errors are related to the spectral resolution when a spectral signal is misinterpreted as water when in reality it is wet soil. The NIR band is prone to commission errors as clusters of wet soil and shadows from microtopography and clouds can be misinterpreted as water. Nevertheless, the cloud shadows problem can be solved with the mingling of R , G , B , and NIR bands (Muster et al. 2013).

Our accuracies are comparable to the results from other studies in Arctic regions (Paltan, Dash, and Edwards 2015; Palmtag et al. 2016; Muster et al. 2017). An accuracy of 77% was obtained by applying the unsupervised k -means classification on Pleiades images with 0.5 m spatial resolution (Muster et al. 2017). For supervised methods, the accuracies ranged from 68% to 97% (Palmtag et al. 2016; Muster et al. 2017). For instance, the accuracy reached 97% for the DS method applied on ALOS Panchromatic Remote – sensing Instrument for Stereo Mapping (PRISM) images with 3 m spatial resolution (Muster et al. 2017). The marked difference is that all these approaches used images with high spatial resolution (≤ 3 m), which made detecting ponds smaller than 100 m^2 possible.

Gislason, Benediktsson, and Sveinsson (2006) tested the RF method for land cover classification on Landsat images and obtained an OA of 82.8%. Clerici, Calderón, and Posada (2017) applied this method on Sentinel-2 images for land cover classification and obtained an OA of just 48.1% and a K of 0.37. By combining the optical image with the radar image (Sentinel-1), the OA slightly increased to 55.5% and K to 0.49 (Clerici, Calderón, and Posada 2017). Recently, this method was adopted in mapping urban lake areas, and obtained an average OA ranging from 94.6% to 99.1% in different time series.

However, 30 m spatial resolution images were used (Landsat and HJ-1A) and only large lakes were analysed (Shi et al. 2019). The RF method has been shown to generate better results in mapping the potential permafrost distribution, as the OA reached 88% (Deluigi, Lambiel, and Kanevski 2017; Wang et al. 2019a). In our case, the RF method reached one of the highest OA (96%) and K (0.88) but also generated large misclassifications.

Statistical results from the regression analysis reveal a close correspondence between OA and K (Figure 4). K and OA are in a positive correlation ($R^2 = 0.88$), as results with high OA have also a high K. In contrast, these accuracy indices do not present any correspondence with the water bodies surfaces area. These happens because several results with high OA and K (>91% and 0.8), presenting also large water surface area (Table S1). Results from MLC and RF methods (e.g. MLC3, MLC8, and RF11) reveal a water body surface area ranging from 25 to 37 km². In these cases, water bodies are properly represented with a commission error below 8%. However, extensive areas of land are misclassified as water as the commission error exceed 20%. There are also results with high OA (91%) and K (0.7) and with a reduced water surface area (< 6 km²) as k-means14, DS12, and DS13. In these situations, the misclassifications are reduced as the commission errors range between 8% and 10% but the omission errors exceed 30%.

MLC method was used in many permafrost areas and provided good results in mapping land cover types, although the accuracies vary on a large range. Grosse, Schirrmeyer, and Malthus (2006) used the MLC approach to quantify terrain types relevant to thermokarst in northern Siberia and achieve an OA of 79%. In northern Alaska, a geomorphology map was developed by using MLC together with Object Based Image Analysis and band thresholding, and obtained an OA of 75% (Lara et al. 2015). MLC used in tandem with DS method was applied on aerial images in the Lena Delta for extracting the land cover types (Muster et al. 2012). Their accuracy ranged from 62% for the overgrown water class to 100% for the open water class, with an OA of 84%. Also, at Chalaping the MLC method of using visible and NIR bands was proven reliable in mapping water bodies. Thereby, it could be transposed to generate inventories on different time periods and images, but also extrapolated to other regions from QTP and beyond.

4.2. Water body abundance and size distribution

Assessing these approaches revealed that the supervised methods reach higher accuracies, but paradoxically large overestimation of the water surface area up to 40 km². Thereby, these methods require a large amount of time for refining the results. Conversely, the unsupervised method and especially the water indices yielded slightly lower accuracies, but also underestimated water surface area. The MLC5 supervised method represents the best compromise solution, having one of the highest accuracies and moderate overestimation of the water surface area.

Pekel et al. (2016) developed a global water bodies inventory based on Landsat images at 30 m spatial resolution acquired from 1984 to 2015. If we compare their maximum water body extent during that period, they identified only 315 water bodies in the Chalaping area, covering 2.5 km² (Figure 7(b)). The MLC5 and NDWI approaches mapped with 651 and 213 more water bodies than in that inventory. As expected, the largest difference occurred in the pond category, where the inventory of Pekel et al. (2016) detected just 279 ponds covering 0.38 km² (Figure 6). Their inventory revealed only two

large lakes and 34 small lakes. In our case, the NDWI method identified 23 more small lakes and with 189 more ponds than the inventory of Pekel et al. (2016) (Figure 6(a)). During the same time, the MLC5 approach mapped 27 more small lakes and 623 more ponds. Thereby, Sentinel-2 images at 10 m spatial resolution better identify ponds smaller as 400 m². In many cases, ponds smaller than 400 m² were reliably mapped but were excluded from the inventory as they were smaller than four pixels.

Pond abundance in this area corresponds well to other areas of the Arctic (Muster et al. 2012, 2013, 2017). Water body inventories in the Arctic region were generally developed for change detection by using the Landsat imagery archive due to its temporal resolution. However, this limited the sizes of mapped water bodies because of image resolution, thus omitting smaller ponds (Walter et al. 2006; Boike et al. 2016; Kravtsova and Rodionova 2016). Inventories developed on high-resolution aerial and satellite imagery (5 m or less) better reveal the abundance of ponds (Andresen and Lougheed 2015; Liljedahl et al. 2016; Muster et al. 2017). A comprehensive example is the Permafrost Region Pond and Lake (PeRL) database in which ponds smaller than 4 m² were mapped for the circum-Arctic region (Muster et al. 2017). In the circum-Arctic region, ponds represent from 45% to 99% of all water bodies (Muster et al. 2017). These results are comparable to our inventory from Chalaping, where the 902 mapped ponds represent 93% of the total water bodies. On regional studies from the QTP, mainly lakes larger than 1 km² were mapped (G. Zhang et al. 2014, 2017; Wan et al. 2016; Lu et al. 2017). Generally, omitting small lakes and ponds leads to large underestimations of water body count and water surface area in permafrost environments. In this context, taking into account the inventory of Pekel et al. (2016), only at Chalaping the water body surface area was underestimated with 2.2 km² ($n = 651$).

Using Sentinel-2 images, our classifications mapped more water bodies with smoother boundaries compared to Landsat images (Figure 7). However, extensive areas of peat, as well as the alpine meadow and drained lakes with high moisture content, introduced significant noises to our classifications. Thus, Sentinel-2 images still represent a coarse resolution to distinguish between small ponds with emerged vegetation and other vegetated areas with high moisture content. Using images with higher resolution (1 m or less) would overcome this problem and map even smaller ponds. Though, to cover large areas it requires numerous high-resolution images that demand high computing power and storage space, and all these implies substantial costs.

5. Conclusions

In this study, we assessed different classification methods (e.g. spectral water indices, supervised and unsupervised classifiers) for mapping water bodies in a small permafrost environment. Comparing these approaches helped to identify MLC as the most suitable method for mapping the water bodies and to improve the regional database for the QTP.

Supervised classifications showed the highest OA (>90%), but revealed large misclassification with water bodies surface area larger than 15 km². Misclassifications are mainly due to the presence of snow, ice, and shadows. NDWI approach showed the lowest water surface area (4.06 km²) but with large underestimations of water bodies, with an omission error of 55.9%. Unsupervised classification (k -means) reported the second least water surface area and was useful for identifying more classes (e.g. grass, ice, bare ground, and shadows).



The MLC5 method applied on visible and NIR bands with two classes represented the compromise solution, in terms of accuracy and water surface area. The MLC5 revealed an OA of 96%, a K of 0.87, and a moderate water surface extent (14.87 km^2) compared to the other classifications results. However, misclassifications are still presented, which requires manual editing. After the refining step, in an area of 150 km^2 at Chalaping, the MLC5 method identified 966 water bodies with a total water surface of 4.7 km^2 . From these, ponds dominate the landscape, comprising 93% of individual water bodies and contribute to 42% of the total water surface. The MLC5 identified 449 more water bodies than the NDWI and with 651 more water bodies than previous inventories in this area, especially in the ponds category. These findings emphasize the contribution of ponds to the total water body count, in light of being omitted from previous water body inventories on the QTP.

This study shows that Sentinel-2 images can correctly detect ponds small as 400 m^2 on the QTB. Moreover, using images with higher spatial resolution than Sentinel-2, the MLC method can identify water bodies at a finer scale and can increase the classification accuracy. Future work in this area should assess temporal variability of water bodies annually for changes in lake area and ice phenology. Applying a change detection approach over the last decades will improve the understanding of water body evolution in relation to warming permafrost in the HAYR.

Results from this study have widespread implications in protecting and monitoring the integrity of wetlands in the Sanjiangyuan National Park of China. Projections of future climate change and water and energy budgets for the QTP should take into account these ponds due to their dominance in the landscape and their significant roles in hydrological and ecological systems.

Acknowledgements

Sentinel-2A data are in the courtesy of European Space Agency (<https://scihub.copernicus.eu/>) and ALOS PALSAR DEM, of Alaska Satellite Facility (<https://www.asf.alaska.edu/>). We express our gratitude to the Editor and two anonymous reviewers for their generous efforts and insightful and constructive feedbacks on an earlier version of this manuscript.

Disclosure statement

No potential conflict of interest was reported by the authors.

Funding

This work was financially supported by the subject of the Strategic Priority Research Program of Chinese Academy of Sciences (CAS) 'Impacts of changing permafrost hydrological processes in the Qilian Mountains on the water supplies and security' (Grant No. XDA20100103); CAS Postdoctoral Program of Dr. Raul-David Ţerban under the auspices of President's International Fellowship Initiative-PIFI (2018PE0007), and; Ministry of Science and Technology of China Key R&D Program (Grant No. 2017YFC0405704) 'Techniques and Equipment for online monitoring of essential hydrological elements in cold regions'

ORCID

- Raul-David Şerban  <http://orcid.org/0000-0003-2924-2735>
 Huijun Jin  <http://orcid.org/0000-0002-8402-7897>
 Mihaela Şerban  <http://orcid.org/0000-0002-0568-3416>
 Dongliang Luo  <http://orcid.org/0000-0001-5844-3638>
 Xiaoying Jin  <http://orcid.org/0000-0002-3831-5839>

References

- Abnizova, A., J. Siemens, M. Langer, and J. Boike. 2012. "Small Ponds with Major Impact: The Relevance of Ponds and Lakes in Permafrost Landscapes to Carbon Dioxide Emissions." *Global Biogeochemical Cycles* 26 (2): 1–9. doi:[10.1029/2011GB004237](https://doi.org/10.1029/2011GB004237).
- Adam, E., O. Mutanga, J. Odindi, and E. M. Abdel-Rahman. 2014. "Land-Use/Cover Classification in a Heterogeneous Coastal Landscape Using RapidEye Imagery: Evaluating the Performance of Random Forest and Support Vector Machines Classifiers." *International Journal of Remote Sensing* 35 (10): 3440–3458. doi:[10.1080/01431161.2014.903435](https://doi.org/10.1080/01431161.2014.903435).
- Andresen, C. G., and V. L. Lougheed. 2015. "Disappearing Arctic Tundra Ponds: Fine-Scale Analysis of Surface Hydrology in Drained Thaw Lake Basins over a 65 Year Period (1948–2013)." *Journal of Geophysical Research: Biogeosciences* 120 (3): 466–479. doi:[10.1002/2014JG002778](https://doi.org/10.1002/2014JG002778).
- Bai, S.-B., J. Wang, G.-N. Lü, P.-G. Zhou, -S.-S. Hou, and S.-N. Xu. 2010. "GIS-Based Logistic Regression for Landslide Susceptibility Mapping of the Zhongxian Segment in the Three Gorges Area, China." *Geomorphology* 115 (1–2): 23–31. doi:[10.1016/j.geomorph.2009.09.025](https://doi.org/10.1016/j.geomorph.2009.09.025).
- Boike, J., T. Grau, B. Heim, F. Günther, M. Langer, S. Muster, I. Gouttevin, and S. Lange. 2016. "Satellite-Derived Changes in the Permafrost Landscape of Central Yakutia, 2000 – 2011: Wetting, Drying, and Fires." *Global and Planetary Change* 139: 116–127. doi:[10.1016/j.gloplacha.2016.01.001](https://doi.org/10.1016/j.gloplacha.2016.01.001).
- Breiman, L. 2001. "Random Forests." *Machine Learning* 45 (1): 5–32. doi:[10.1023/A:1010933404324](https://doi.org/10.1023/A:1010933404324).
- Burges, C. J. C. 1998. "A Tutorial on Support Vector Machines for Pattern Recognition." *Data Mining and Knowledge Discovery* 2: 121–167. doi:[10.1023/A:1009715923555](https://doi.org/10.1023/A:1009715923555).
- Carroll, M. L., J. R. G. Townshend, C. M. Dimiceli, T. Loboda, and R. A. Sohlberg. 2011. "Shrinking Lakes of the Arctic: Spatial Relationships and Trajectory of Change." *Geophysical Research Letters* 38: L20406. doi:[10.1029/2011GL049427](https://doi.org/10.1029/2011GL049427).
- Clerici, N., C. A. V. Calderón, and J. M. Posada. 2017. "Fusion of Sentinel-1A and Sentinel-2A Data for Land Cover Mapping: A Case Study in the Lower Magdalena Region, Colombia." *Journal of Maps* 13 (2): 718–726. doi:[10.1080/17445647.2017.1372316](https://doi.org/10.1080/17445647.2017.1372316).
- Congalton, R. G. 1991. "A Review of Assessing the Accuracy of Classifications of Remotely Sensed Data." *Remote Sensing of Environment* 37: 35–46. doi:[10.1103/PhysRevE.87.021001](https://doi.org/10.1103/PhysRevE.87.021001).
- Cooley, S. W., L. C. Smith, J. C. Ryan, L. H. Pitcher, and T. M. Pavelsky. 2019. "Arctic-Boreal Lake Dynamics Revealed Using CubeSat Imagery." *Geophysical Research Letters* 46 (4): 2111–2120. doi:[10.1029/2018GL081584](https://doi.org/10.1029/2018GL081584).
- Debeer, C. M., H. S. Wheater, W. L. Quinton, S. K. Carey, R. E. Stewart, M. D. MacKay, and P. Marsh. 2015. "The Changing Cold Regions Network: Observation, Diagnosis and Prediction of Environmental Change in the Saskatchewan and Mackenzie River Basins, Canada." *Science China Earth Sciences* 58 (1): 46–60. doi:[10.1007/s11430-014-5001-6](https://doi.org/10.1007/s11430-014-5001-6).
- Deluigi, N., C. Lambiel, and M. Kanevski. 2017. "Data-Driven Mapping of the Potential Mountain Permafrost Distribution." *Science of the Total Environment* 590–591: 370–380. doi:[10.1016/j.scitotenv.2017.02.041](https://doi.org/10.1016/j.scitotenv.2017.02.041).
- Du, Y., Y. Zhang, F. Ling, Q. Wang, W. Li, and X. Li. 2016. "Water Bodies' Mapping from Sentinel-2 Imagery with Modified Normalized Difference Water Index at 10-m Spatial Resolution Produced by Sharpening the SWIR Band." *Remote Sensing* 8 (4): 354. doi:[10.3390/rs8040354](https://doi.org/10.3390/rs8040354).

- Euskirchen, E. S., A. D. McGuire, D. W. Kicklighter, Q. Zhuang, J. S. Clein, R. J. Dargaville, D. G. Dye, et al. 2006. "Importance of Recent Shifts in Soil Thermal Dynamics on Growing Season Length, Productivity, and Carbon Sequestration in Terrestrial High-Latitude Ecosystems." *Global Change Biology* 12 (4): 731–750. doi:[10.1111/j.1365-2486.2006.01113.x](https://doi.org/10.1111/j.1365-2486.2006.01113.x).
- Frantz, D., E. Haß, A. Uhl, J. Stoffels, and J. Hill. 2018. "Improvement of the Fmask Algorithm for Sentinel-2 Images: Separating Clouds from Bright Surfaces Based on Parallax Effects." *Remote Sensing of Environment* 215: 471–481. doi:[10.1016/j.rse.2018.04.046](https://doi.org/10.1016/j.rse.2018.04.046).
- Ghorbanzadeh, O., T. Blaschke, K. Gholamnia, S. R. Meena, D. Tiede, and J. Aryal. 2019. "Evaluation of Different Machine Learning Methods and Deep-Learning Convolutional Neural Networks for Landslide Detection." *Remote Sensing* 11 (2): 196. doi:[10.3390/rs11020196](https://doi.org/10.3390/rs11020196).
- Gislason, P. O., J. A. Benediktsson, and J. R. Sveinsson. 2006. "Random Forests for Land Cover Classification." *Pattern Recognition Letters* 27 (4): 294–300. doi:[10.1016/j.patrec.2005.08.011](https://doi.org/10.1016/j.patrec.2005.08.011).
- Grosse, G., L. Schirrmeister, and T. J. Malthus. 2006. "Application of Landsat-7 Satellite Data and a DEM for the Quantification of Thermokarst-Affected Terrain Types in the Periglacial Lena-Anabar Coastal Lowland." *Polar Research* 25 (1): 51–67. doi:[10.1111/j.1751-8369.2006.tb00150.x](https://doi.org/10.1111/j.1751-8369.2006.tb00150.x).
- Guo, W., S. Liu, J. Xu, L. Wu, D. Shangguan, X. Yao, J. Wei, et al. 2015. "The Second Chinese Glacier Inventory: Data, Methods and Results." *Journal of Glaciology* 61 (226): 357–372. doi:[10.3189/2015JoG14J209](https://doi.org/10.3189/2015JoG14J209).
- Janik, P., and T. Lobos. 2006. "Automated Classification of Power-Quality Disturbances Using SVM and RBF Networks." *IEEE Transactions on Power Delivery* 21 (3): 1663–1669. doi:[10.1109/TPWRD.2006.874114](https://doi.org/10.1109/TPWRD.2006.874114).
- Jin, H., R. He, G. Cheng, Q. Wu, S. Wang, L. Lü, and X. Chang. 2009. "Changes in Frozen Ground in the Source Area of the Yellow River on the Qinghai-Tibet Plateau, China, and Their Eco-Environmental Impacts." *Environmental Research Letters* 4: 1–11. doi:[10.1088/1748-9326/4/4/045206](https://doi.org/10.1088/1748-9326/4/4/045206).
- Johansen, B., and H. Tømmervik. 2014. "The Relationship between Phytomass, NDVI and Vegetation Communities on Svalbard." *International Journal of Applied Earth Observation and Geoinformation* 27: 20–30. doi:[10.1016/j.jag.2013.07.001](https://doi.org/10.1016/j.jag.2013.07.001).
- Jones, B. M., G. Grosse, C. D. Arp, M. C. Jones, K. M. Walter Anthony, and V. E. Romanovsky. 2011. "Modern Thermokarst Lake Dynamics in the Continuous Permafrost Zone, Northern Seward Peninsula, Alaska." *Journal of Geophysical Research: Biogeosciences* 116 (3): 1–13. doi:[10.1029/2011JG001666](https://doi.org/10.1029/2011JG001666).
- Knight, A. W., D. R. Tindall, and B. A. Wilson. 2009. "A Multitemporal Multiple Density Slice Method for Wetland Mapping across the State of Queensland, Australia." *International Journal of Remote Sensing* 30 (13): 3365–3392. doi:[10.1080/01431160802562180](https://doi.org/10.1080/01431160802562180).
- Kratvsova, V. I., and T. V. Rodionova. 2016. "Variations in Size and Number of Thermokarst Lakes in Different Permafrost Regions: Spaceborne Evidence." *Scientific Journal Earth's Cryosphere* XX 1: 75–81.
- Kuhn, M., E. J. Lundin, R. Giesler, M. Johansson, and J. Karlsson. 2018. "Emissions from Thaw Ponds Largely Offset the Carbon Sink of Northern Permafrost Wetlands." *Scientific Reports* 8 (1): 1–7. doi:[10.1038/s41598-018-27770-x](https://doi.org/10.1038/s41598-018-27770-x).
- Landis, J. R., and G. G. Koch. 1977. "The Measurement of Observer Agreement for Categorical Data." *Biometrics* 33 (1): 159–174. doi:[10.2307/2529310](https://doi.org/10.2307/2529310).
- Lara, M. J., A. D. McGuire, E. S. Euskirchen, C. E. Tweedie, K. M. Hinkel, A. N. Skurikhin, V. E. Romanovsky, G. Grosse, W. R. Bolton, and H. Genet. 2015. "Polygonal Tundra Geomorphological Change in Response to Warming Alters Future CO₂ and CH₄ Flux on the Barrow Peninsula." *Global Change Biology* 21 (4): 1634–1651. doi:[10.1111/gcb.12757](https://doi.org/10.1111/gcb.12757).
- Laurion, I., W. F. Vincent, S. MacIntyre, L. Retamal, C. Dupont, P. Francus, and R. Pienitz. 2010. "Variability in Greenhouse Gas Emissions from Permafrost Thaw Ponds." *Limnology and Oceanography* 55 (1): 115–133. doi:[10.4319/lo.2010.55.1.0115](https://doi.org/10.4319/lo.2010.55.1.0115).
- Li, J., T. A. Warner, Y. Wang, J. Bai, and A. Bao. 2019. "Mapping Glacial Lakes Partially Obscured by Mountain Shadows for Time Series and Regional Mapping Applications." *International Journal of Remote Sensing* 40 (2): 615–641. doi:[10.1080/01431161.2018.1516314](https://doi.org/10.1080/01431161.2018.1516314).

- Li, W., Z. Du, F. Ling, D. Zhou, H. Wang, Y. Gui, B. Sun, and X. Zhang. 2013. "A Comparison of Land Surface Water Mapping Using the Normalized Difference Water Index from TM, ETM+ and ALI." *Remote Sensing* 5 (11): 5530–5549. doi:[10.3390/rs5115530](https://doi.org/10.3390/rs5115530).
- Liljedahl, A. K., J. Boike, R. P. Daanen, A. N. Fedorov, G. V. Frost, G. Grosse, L. D. Hinzman, et al. 2016. "Pan-Arctic Ice-Wedge Degradation in Warming Permafrost and Its Influence on Tundra Hydrology." *Nature Geoscience* 9 (4): 312–318. doi:[10.1038/ngeo2674](https://doi.org/10.1038/ngeo2674).
- Lillesand, T., R. W. Kiefer, and J. Chipman. 2004. *Remote Sensing and Image Interpretation*. 5th ed. New York: John Wiley & Sons.
- Löw, F., U. Michel, S. Dech, and C. Conrad. 2013. "Impact of Feature Selection on the Accuracy and Spatial Uncertainty of Per-Field Crop Classification Using Support Vector Machines." *ISPRS Journal of Photogrammetry and Remote Sensing* 85: 102–119. doi:[10.1016/j.isprsjprs.2013.08.007](https://doi.org/10.1016/j.isprsjprs.2013.08.007).
- Lu, S., L. Jia, L. Zhang, Y. Wei, M. H. A. Baig, Z. Zhai, J. Meng, X. Li, and G. Zhang. 2017. "Lake Water Surface Mapping in the Tibetan Plateau Using the MODIS MOD09Q1 Product." *Remote Sensing Letters* 8 (3): 224–233. doi:[10.1080/2150704X.2016.1260178](https://doi.org/10.1080/2150704X.2016.1260178).
- Luo, D., H. Jin, Q. Wu, V. F. Bense, R. He, Q. Ma, S. Gao, X. Jin, and L. Lü. 2018b. "Thermal Regime of Warm-Dry Permafrost in Relation to Ground Surface Temperature in the Source Areas of the Yangtze and Yellow Rivers on the Qinghai-Tibet Plateau, SW China." *Science of the Total Environment* 618: 1033–1045. doi:[10.1016/j.scitotenv.2017.09.083](https://doi.org/10.1016/j.scitotenv.2017.09.083).
- Luo, D., H. Jin, R. He, X. Wang, R. Muskett, and S. Marchenko. 2018a. "Characteristics of Water-Heat Exchanges and Inconsistent Surface Temperature Changes at an Elevational Permafrost Site on the Qinghai-Tibet Plateau." *Journal of Geophysical Research: Atmospheres* 123: 10,057–10,075. doi:[10.1029/2018JD028298](https://doi.org/10.1029/2018JD028298).
- Luo, D., L. Liu, H. Jin, X. Wang, and F. Chen. 2020. "Characteristics of Ground Surface Temperature at Chalaping in the Source Area of the Yellow River, Northeastern Tibetan Plateau." *Agricultural and Forest Meteorology* 281: 107819. doi: [10.1016/j.agrformet.2019.107819](https://doi.org/10.1016/j.agrformet.2019.107819).
- Luo, J., F. Niu, Z. Lin, M. Liu, and G. Yin. 2015. "Thermokarst Lake Changes between 1969 and 2010 in the Beilu River Basin, Qinghai-Tibet Plateau, China." *Science Bulletin* 60 (5): 556–564. doi:[10.1007/s11434-015-0730-2](https://doi.org/10.1007/s11434-015-0730-2).
- Lv, W., Q. Yu, and W. Yu. 2010. "Water Extraction in SAR Images Using GLCM and Support Vector Machine." *International Conference on Signal Processing Proceedings, ICSP 2010*, Beijing: 740–743. doi:[10.1109/ICOSP.2010.5655766](https://doi.org/10.1109/ICOSP.2010.5655766).
- Main-Knorn, M., B. Pflug, V. Debaecker, and J. Louis. 2015. "Calibration and Validation Plan for the L2A Processor and Products of the Sentinel-2 Mission." In *International Archives of the Photogrammetry, Remote Sensing and Spatial Information Sciences - ISPRS Archives* 40: 1249–1255. doi:[10.5194/isprarchives-XL-7-W3-1249-2015](https://doi.org/10.5194/isprarchives-XL-7-W3-1249-2015).
- McFeeters, S. K. 1996. "The Use of the Normalized Difference Water Index (NDWI) in the Delineation of Open Water Features." *International Journal of Remote Sensing* 17 (7): 1425–1432. doi:[10.1080/01431169608948714](https://doi.org/10.1080/01431169608948714).
- McGuire, A. D., L. G. Anderson, T. R. Christensen, S. Dallimore, L. Guo, D. J. Hayes, M. Heimann, T. D. Lorenson, R. W. Macdonald, and N. Roulet. 2009. "Sensitivity of the Carbon Cycle in the Arctic to Climate Change." *Ecological Monographs* 79 (4): 523–555. doi:[10.1890/08-2025.1](https://doi.org/10.1890/08-2025.1).
- Muster, S., B. Heim, A. Abnizova, and J. Boike. 2013. "Water Body Distributions across Scales: A Remote Sensing Based Comparison of Three Arctic Tundrawetlands." *Remote Sensing* 5 (4): 1498–1523. doi:[10.3390/rs5041498](https://doi.org/10.3390/rs5041498).
- Muster, S., K. Roth, M. Langer, S. Lange, F. Cresto Aleina, A. Bartsch, A. Morgenstern, et al. 2017. "PeRL: A Circum-Arctic Permafrost Region Pond and Lake Database." *Earth System Science Data* 9 (1): 317–348. doi:[10.5194/essd-9-317-2017](https://doi.org/10.5194/essd-9-317-2017).
- Muster, S., M. Langer, B. Heim, S. Westermann, and J. Boike. 2012. "Subpixel Heterogeneity of Ice-Wedge Polygonal Tundra: A Multi-Scale Analysis of Land Cover and Evapotranspiration in the Lena River Delta, Siberia." *Tellus B: Chemical and Physical Meteorology* 64 (1): 17301. doi:[10.3402/tellusb.v64i0.17301](https://doi.org/10.3402/tellusb.v64i0.17301).



- Nitze, I., U. Schulthess, and H. Asche. 2012. "Comparison of Machine Learning Algorithms Random Forest, Artificial Neuronal Network and Support Vector Machine to Maximum Likelihood for Supervised Crop Type Classification." *Proceedings of the 4th Conference on GEographic Object-Based Image Analysis – GEOBIA 2012*, Rio de Janeiro: 35–40.
- Pal, M., and G. M. Foody. 2012. "Evaluation of SVM, RVM and SMLR for Accurate Image Classification with Limited Ground Data." *IEEE Journal of Selected Topics in Applied Earth Observations and Remote Sensing* 5 (5): 1344–1355. doi:[10.1109/JSTARS.2012.2215310](https://doi.org/10.1109/JSTARS.2012.2215310).
- Palmtag, J., J. Ramage, G. Hugelius, N. Gentsch, N. Lashchinskiy, A. Richter, and P. Kuhry. 2016. "Controls on the Storage of Organic Carbon in Permafrost Soil in Northern Siberia." *European Journal of Soil Science* 67 (4): 478–491. doi:[10.1111/ejss.12357](https://doi.org/10.1111/ejss.12357).
- Paltan, H., J. Dash, and M. Edwards. 2015. "A Refined Mapping of Arctic Lakes Using Landsat Imagery." *International Journal of Remote Sensing* 36 (23): 5970–5982. doi:[10.1080/01431161.2015.1110263](https://doi.org/10.1080/01431161.2015.1110263).
- Pekel, J.-F., A. Cottam, N. Gorelick, and A. S. Belward. 2016. "High-Resolution Mapping of Global Surface Water and Its Long-Term Changes." *Nature* 540 (7633): 418–422. doi:[10.1038/nature20584](https://doi.org/10.1038/nature20584).
- Peters, J., B. De Baets, N. E. C. Verhoest, R. Samson, S. Degroeve, P. De Becker, and W. Huybrechts. 2007. "Random Forests as a Tool for Ecohydrological Distribution Modelling." *Ecological Modelling* 207 (2–4): 304–318. doi:[10.1016/j.ecolmodel.2007.05.011](https://doi.org/10.1016/j.ecolmodel.2007.05.011).
- Qiao, B., L. Zhu, and R. Yang. 2019. "Temporal-Spatial Differences in Lake Water Storage Changes and Their Links to Climate Change Throughout the Tibetan Plateau." *Remote Sensing of Environment* 222 (October 2017): 232–243. doi:[10.1016/j.rse.2018.12.037](https://doi.org/10.1016/j.rse.2018.12.037).
- Räsänen, A., V. Elsakov, and T. Virtanen. 2019. "Usability of One-Class Classification in Mapping and Detecting Changes in Bare Peat Surfaces in the Tundra." *International Journal of Remote Sensing* 40 (11): 4083–4103. doi:[10.1080/01431161.2018.1558376](https://doi.org/10.1080/01431161.2018.1558376).
- Rautio, M., F. Dufresne, I. Laurion, S. Bonilla, W. F. Vincent, and K. S. Christoffersen. 2011. "Shallow Freshwater Ecosystems of the Circumpolar Arctic." *Écoscience* 18 (3): 204–222. doi:[10.2980/18-3-3463](https://doi.org/10.2980/18-3-3463).
- Rokni, K., A. Ahmad, K. Solaimani, and S. Hazini. 2015. "A New Approach for Surface Water Change Detection: Integration of Pixel Level Image Fusion and Image Classification Techniques." *International Journal of Applied Earth Observation and Geoinformation* 34 (1): 226–234. doi:[10.1016/j.jag.2014.08.014](https://doi.org/10.1016/j.jag.2014.08.014).
- Schneider, J., G. Grosse, and D. Wagner. 2009. "Land Cover Classification of Tundra Environments in the Arctic Lena Delta Based on Landsat 7 ETM+ Data and Its Application for Upscaling of Methane Emissions." *Remote Sensing of Environment* 113 (2): 380–391. doi:[10.1016/j.rse.2008.10.013](https://doi.org/10.1016/j.rse.2008.10.013).
- Shi, L., F. Ling, G. M. Foody, C. Chen, S. Fang, X. Li, Y. Zhang, and Y. Du. 2019. "Permanent Disappearance and Seasonal Fluctuation of Urban Lake Area in Wuhan, China Monitored with Long Time Series Remotely Sensed Images from 1987 to 2016." *International Journal of Remote Sensing* 40 (22): 8484–8505. doi:[10.1080/01431161.2019.1612119](https://doi.org/10.1080/01431161.2019.1612119).
- Singh, K. V., R. Setia, S. Sahoo, A. Prasad, and B. Pateriya. 2015. "Evaluation of NDWI and MNDWI for Assessment of Waterlogging by Integrating Digital Elevation Model and Groundwater Level." *Geocarto International* 30 (6): 650–661. doi:[10.1080/10106049.2014.965757](https://doi.org/10.1080/10106049.2014.965757).
- Smol, J. P., and M. S. V. Douglas. 2007. "Crossing the Final Ecological Threshold in High Arctic Ponds." *Proceedings of the National Academy of Sciences* 104 (30): 12395–12397. doi:[10.1073/pnas.0702777104](https://doi.org/10.1073/pnas.0702777104).
- Song, C., B. Huang, L. Ke, and K. S. Richards. 2014. "Remote Sensing of Alpine Lake Water Environment Changes on the Tibetan Plateau and Surroundings: A Review." *ISPRS Journal of Photogrammetry and Remote Sensing* 92: 26–37. doi:[10.1016/j.isprsjprs.2014.03.001](https://doi.org/10.1016/j.isprsjprs.2014.03.001).
- Sun, J., T. Zhou, M. Liu, Y. Chen, H. Shang, L. Zhu, A. A. Shedai, et al. 2018. "Linkages of the Dynamics of Glaciers and Lakes with the Climate Elements over the Tibetan Plateau." *Earth-Science Reviews* 185 (June): 308–324. doi:[10.1016/j.earscirev.2018.06.012](https://doi.org/10.1016/j.earscirev.2018.06.012).

- Tien Bui, D., T. A. Tuan, H. Klempe, B. Pradhan, and I. Revhaug. 2016. "Spatial Prediction Models for Shallow Landslide Hazards: A Comparative Assessment of the Efficacy of Support Vector Machines, Artificial Neural Networks, Kernel Logistic Regression, and Logistic Model Tree." *Landslides* 13 (2): 361–378. doi:[10.1007/s10346-015-0557-6](https://doi.org/10.1007/s10346-015-0557-6).
- Van Den Eeckhaut, M., T. Vanwalleghem, J. Poesen, G. Govers, G. Verstraeten, and L. Vandekerckhove. 2006. "Prediction of Landslide Susceptibility Using Rare Events Logistic Regression: A Case-Study in the Flemish Ardennes (Belgium)." *Geomorphology* 76 (3–4): 392–410. doi:[10.1016/j.geomorph.2005.12.003](https://doi.org/10.1016/j.geomorph.2005.12.003).
- Vapnik, V. N. 1999. "An Overview of Statistical Learning Theory." *IEEE Transactions on Neural Networks* 10 (5): 988–999. doi:[10.1109/72.788640](https://doi.org/10.1109/72.788640).
- Veronesi, F., and L. Hurni. 2014. "Random Forest with Semantic Tie Points for Classifying Landforms and Creating Rigorous Shaded Relief Representations." *Geomorphology* 224: 152–160. doi:[10.1016/j.geomorph.2014.07.020](https://doi.org/10.1016/j.geomorph.2014.07.020).
- Verpoorter, C., T. Kutser, and L. Tranvik. 2012. "Automated Mapping of Water Bodies Using Landsat Multispectral Data." *Limnology and Oceanography: Methods* 10 (DECEMBER): 1037–1050. doi:[10.4319/lom.2012.10.1037](https://doi.org/10.4319/lom.2012.10.1037).
- Walter, K. M., S. A. Zimov, J. P. Chanton, D. Verbyla, and F. S. Chapin. 2006. "Methane Bubbling from Siberian Thaw Lakes as a Positive Feedback to Climate Warming." *Nature* 443 (7107): 71–75. doi:[10.1038/nature05040](https://doi.org/10.1038/nature05040).
- Wan, W., D. Long, Y. Hong, Y. Ma, Y. Yuan, P. Xiao, H. Duan, Z. Han, and X. Gu. 2016. "A Lake Data Set for the Tibetan Plateau from the 1960s, 2005, and 2014." *Scientific Data* 3: 1–13. doi:[10.1038/sdata.2016.39](https://doi.org/10.1038/sdata.2016.39).
- Wang, T. D., Y. B. Fang, W. Yang, Y. Qin, and Y. Wang. 2019a. "Data-Driven Mapping of the Spatial Distribution and Potential Changes of Frozen Ground over the Tibetan Plateau." *Science of the Total Environment* 649: 515–525. doi:[10.1016/j.scitotenv.2018.08.369](https://doi.org/10.1016/j.scitotenv.2018.08.369).
- Wang, T. T., W. P. Wang, R. Li, C. Xie, and D. Zou. 2019b. "Spatial Distribution and Changes of Permafrost on the Qinghai-Tibet Plateau Revealed by Statistical Models during the Period of 1980 to 2010." *Science of the Total Environment* 650: 661–670. doi:[10.1016/j.scitotenv.2018.08.398](https://doi.org/10.1016/j.scitotenv.2018.08.398).
- Wang, X., and L. Xu. 2018. "Waterbodies Extraction from Landsat8-Oli Imagery Using a Water Index-Guided Stochastic Fully-Connected Conditional Random Field Model and the Support Vector Machine." *International Archives of the Photogrammetry, Remote Sensing and Spatial Information Sciences - ISPRS Archives* 42: 1789–1794. doi:[10.5194/isprs-archives-XLII-3-1789-2018](https://doi.org/10.5194/isprs-archives-XLII-3-1789-2018).
- Williamson, A. G., A. F. Banwell, I. C. Willis, and N. S. Arnold. 2018. "Dual-Satellite (Sentinel-2 and Landsat 8) Remote Sensing of Supraglacial Lakes in Greenland." *Cryosphere* 12 (9): 3045–3065.
- Wu, X., Z. Nan, S. Zhao, L. Zhao, and G. Cheng. 2018. "Spatial Modeling of Permafrost Distribution and Properties on the Qinghai-Tibet Plateau." *Permafrost and Periglacial Processes* 29 (2): 86–89. doi:[10.1002/ppp.1971](https://doi.org/10.1002/ppp.1971).
- Xu, H. 2006. "Modification of Normalised Difference Water Index (NDWI) to Enhance Open Water Features in Remotely Sensed Imagery." *International Journal of Remote Sensing* 27 (14): 3025–3033. doi:[10.1080/01431160600589179](https://doi.org/10.1080/01431160600589179).
- Yang, Y., Y. Liu, M. Zhou, S. Zhang, W. Zhan, C. Sun, and Y. Duan. 2015. "Landsat 8 OLI Image Based Terrestrial Water Extraction from Heterogeneous Backgrounds Using a Reflectance Homogenization Approach." *Remote Sensing of Environment* 171: 14–32. doi:[10.1016/j.rse.2015.10.005](https://doi.org/10.1016/j.rse.2015.10.005).
- Yoshikawa, K., and L. D. Hinzman. 2003. "Shrinking Thermokarst Ponds and Groundwater Dynamics in Discontinuous Permafrost near Council, Alaska." *Permafrost and Periglacial Processes* 14 (2): 151–160. doi:[10.1002/ppp.451](https://doi.org/10.1002/ppp.451).
- Zhang, G., J. Li, and G. Zheng. 2017. "Lake-Area Mapping in the Tibetan Plateau: An Evaluation of Data and Methods." *International Journal of Remote Sensing* 38 (3): 742–772. doi:[10.1080/01431161.2016.1271478](https://doi.org/10.1080/01431161.2016.1271478).

- Zhang, G., T. Yao, C. K. Shum, S. Yi, K. Yang, H. Xie, W. Feng, et al. 2017. "Lake Volume and Groundwater Storage Variations in Tibetan Plateau's Endorheic Basin." *Geophysical Research Letters* 44 (11): 5550–5560. doi:[10.1002/2017GL073773](https://doi.org/10.1002/2017GL073773).
- Zhang, G., T. Yao, H. Xie, K. Zhang, and F. Zhu. 2014. "Lakes' State and Abundance across the Tibetan Plateau." *Chinese Science Bulletin*. doi:[10.1007/s11434-014-0258-x](https://doi.org/10.1007/s11434-014-0258-x).
- Zhang, G., T. Yao, H. Xie, W. Wang, and W. Yang. 2015. "An Inventory of Glacial Lakes in the Third Pole Region and Their Changes in Response to Global Warming." *Global and Planetary Change* 131: 148–157. doi:[10.1016/J.GLOPLACHA.2015.05.013](https://doi.org/10.1016/J.GLOPLACHA.2015.05.013).
- Zhang, M., F. Chen, and B. Tian. 2018. "Glacial Lake Detection from GaoFen-2 Multispectral Imagery Using an Integrated Nonlocal Active Contour Approach: A Case Study of the Altai Mountains, Northern Xinjiang Province." *Water (Switzerland)* 10 (4): 1–17. doi:[10.3390/w10040455](https://doi.org/10.3390/w10040455).